The International Journal of Advanced Manufacturing Technology (2018) 95:4645–4657
https://doi.org/10.1007/s00170-017-1498-0

ORIGINAL ARTICLE

A novel Lap-MRF method for large aperture mirrors

Feng Guan[1,2] · Hao Hu[1,2] · Shengyi Li[1,2] · Zhongyan Liu[1] · Xiaoqiang Peng[1,2] · Feng Shi[1,2]

Received: 15 May 2017 / Accepted: 17 December 2017 / Published online: 16 January 2018

Abstract

A novel magnetorheological finishing (MRF) method, which is named Lap-MRF, is proposed in this paper. The magnetorheological fluid (MR fluid) in the polishing zones can be renewed continuously so that the determinacy is ensured. A lap, instead of a large polishing wheel, is used to expand the polishing area, which improves the material removal rate largely. Lap-MRF uses flexible MR fluid as polishing pad to match the surface well. Moreover, the polishing pad executes planetary motion so as to obtain smooth surface. In this paper, the principle of Lap-MRF and the theoretical model of material removal rate are presented. Using the finite element analysis method, the permanent magnet unit is simulated and a multi-parameter optimization is conducted to improve the performance of Lap-MRF. Finally, a series of polishing experiments and simulation process are carried out. For K9 sample, the volume removal rate is up to 0.76 mm^3/min and its relative change rate is less than 5.5%. For silicon modification layer sample, the surface roughness is improved to 0.788 nm RMS (root mean square) from 1.610 nm RMS. There is no deep pit and the polishing ripple is not apparent on the surface. For Φ1000 mm flat mirror, the convergence efficiency of simulation process is up to 97.2%. These results verify the validity of the proposed method, which makes Lap-MRF to be a promising finishing technology for large aperture mirrors.

Keywords Lap-MRF · Material removal rate · Magnetostatic simulation · Multi-objective optimization · Surface roughness

1 Introduction

With the development of information technology, electronics, aerospace, and national defense, the demands for large aperture optical components are growing rapidly. However, the fabrication difficulty increases greatly because of its special geometry and the high requirements for surface error as well as roughness, which has become one of the key factors restricting the wide use of these components.

Nowadays, the main processing technologies of large aperture mirrors include computer-controlled optical surfacing (CCOS) [1], stressed-lap polishing [2], magnetorheological finishing (MRF), ion beam figuring, [3] and so on. For CCOS, the material removal rate is very high and the RMS value of surface roughness after polishing is very small. However, the polishing lap wears easily and the polishing tool cannot match the mirror well, which makes the material removal rate unstable and the convergence efficiency low [4, 5]. For MRF, the circulating MR fluid is continuously monitored and maintained so that the polishing tool does not wear, which makes the removal function stable [6–8]. Besides, MRF has no subsurface damage. However, the MR fluid flow direction is single so that there exists surface ripple inside MRF spot and there may be deep pits that are polished into a comet-like form by the MR fluid when polishing soft material, which increases the RMS value of surface roughness [9]. Moreover, the material removal rate is restricted since a higher removal rate needs a larger wheel which is extremely demanding in terms of precision machining and assembly [10].

Several scholars have done many researches on the development of new MR fluid-based finishing processes in recent years. Ren et al. proposed a new Belt-MRF with the assistance of belt instead of large wheel to expand the polishing length, which improves the material removal rate [10]. The structure and operating principle were presented and the material removal stability was verified. However, there still exists polishing ripple on the surface after polishing using Belt-MRF. Pan et al.

✉ Hao Hu
tiny_hh@139.com

[1] College of Mechatronic Engineering and Automation, National University of Defense Technology, Changsha 410073, China

[2] Hu'nan Key Laboratory of Ultra-precision Machining Technology, Changsha 410073, China

Fig. 1 Schematic diagram of Lap-MRF

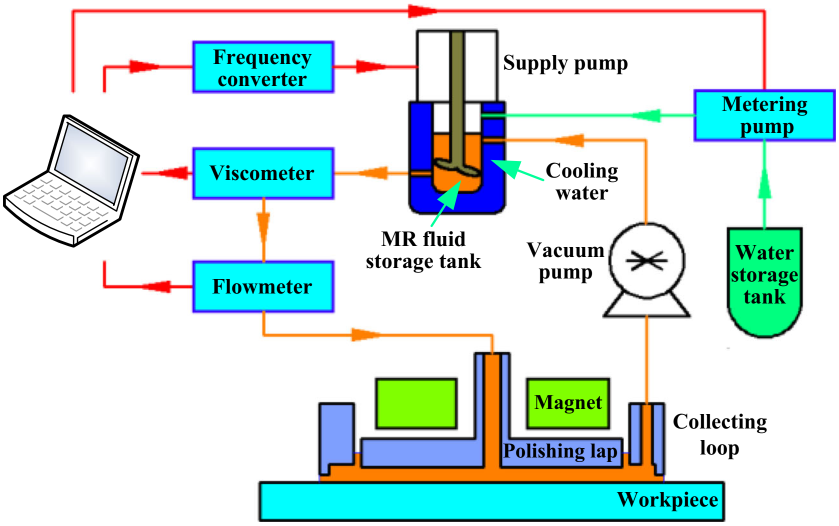

proposed a cluster magnetorheological plane polishing process based on a combination of MRF and cluster mechanism [11, 12]. The magnetic field of a cluster MR disk was simulated and the material removal model was established. Guo et al. developed a kind of clitella MRF, which is based on the "area-contact" polishing ideas, to achieve efficient processing of the optical components [13]. The annulus magnetic field was designed, simulated, and analyzed. Also, some new process methods, such as ball end magnetorheological finishing process [14], magnetorheological abrasive flow finishing process [15, 16], and magnetic compound fluid slurry polishing [17], were developed recently. However, the material removal stability in the finishing processes mentioned above has not been reported yet.

In this paper, we propose a kind of new polishing technology, named Lap-MRF, which combines the advantages of CCOS and MRF. In this method, a lap, instead of a large polishing wheel, is used to expand the polishing area, which makes the material removal rate higher. The circulating MR fluid is well monitored and maintained, the working gap distance is well controlled, and the flexible MR fluid can match the surface well, which ensures the stability of the material removal rate. Moreover, Lap-MRF uses flexible MR fluid as polishing pad and the polishing pad can execute planetary motion so that smooth surface can be obtained. The principle of Lap-MRF, the theoretical model of material removal rate, the simulation and optimization of the permanent magnet unit, the polishing experiments, and simulation process will be discussed in detail in the following sections.

2 Principle of Lap-MRF

This section introduces the principle of Lap-MRF. The schematic diagram of Lap-MRF is shown in Fig. 1. The MR fluid is stored in the MR fluid storage tank, whose temperature is well controlled by the circulating cooling water. When the system functions, the MR fluid is injected into the gap

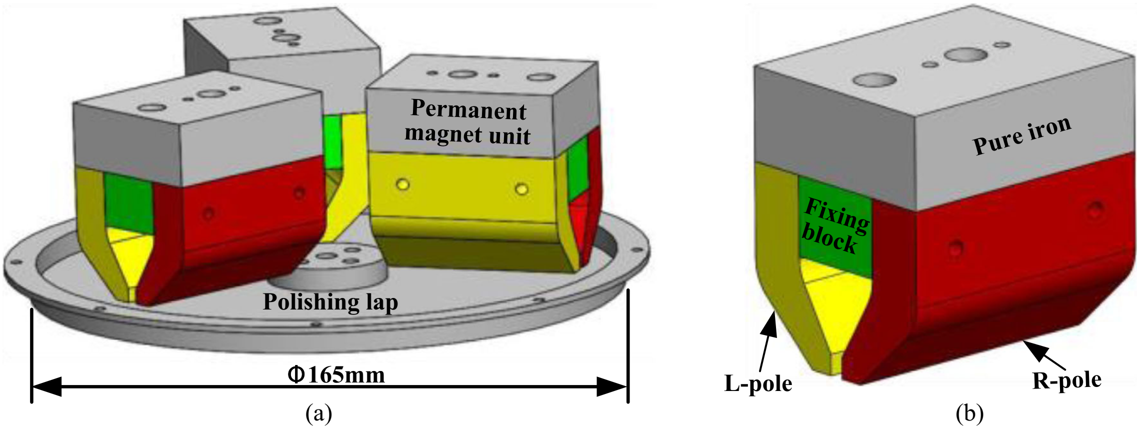

Fig. 2 Polishing head of Lap-MRF. **a** Distribution of permanent magnet unit. **b** Permanent magnet unit

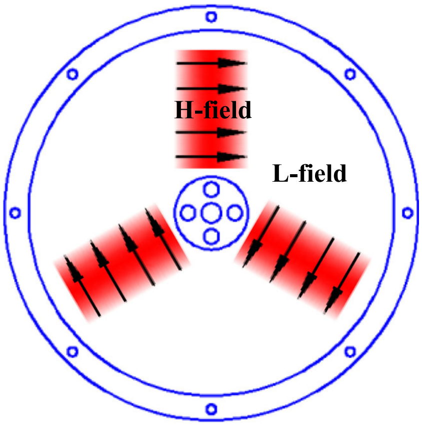

Fig. 3 Distribution of high-intensity and low-intensity magnetic field

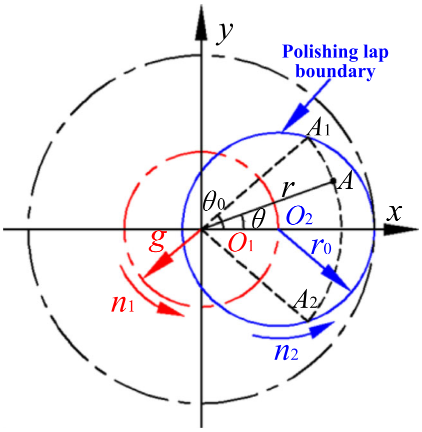

Fig. 4 The kinematic relation between polishing lap and workpiece

between the polishing lap and the workpiece by the supply pump. The MR fluid flows through the gap along the radial direction, and it is sucked by the collecting loop. In the end, the MR fluid moves back into the tank. The flow rate and viscosity of the MR fluid are monitored and adjusted according to the feedback parameters of flowmeter and viscometer, respectively. All these form a complete closed-loop automatic control system.

Figure 2a shows that there are three permanent magnet units over the back of polishing lap along the circumferential direction. As Fig. 2b shows, the permanent magnet unit consists of left and right magnetic poles (L-pole and R-pole), fixing block and pure iron. It can generate high-intensity magnetic field (H-field) zone in the vicinity of the gap as shown in Fig. 3. The fixing block, whose material is aluminum alloy, is just used to fix the two magnetic poles. The MR fluid can flow along the radial direction in the low-intensity magnetic field (L-field) zones so that it can be renewed continuously. Meanwhile, the MR fluid, which is driven by the rotation of the polishing lap, can also flow along the circumferential direction. Therefore, the MR fluid can be renewed continuously in the whole gap between the polishing lap and the workpiece.

The MR fluid flows across the H-field and L-field zones alternatively. When it flows into the H-field zones, it comes into a viscoplastic Bingham medium and forms flexible polishing pad, which results in generation of high shear stress and material removal over the portion of the workpiece.

In order to meet the requirement of material removal stability, MR fluid should be renewed stably and continuously. The fluidity of MR fluid in the L-field zones is a key factor influencing the renewal. Therefore, it is necessary to ensure the magnetic field intensity is as weak as possible in the L-field zones.

Fig. 5 Permanent magnet unit. **a** Special paths surrounding permanent magnet unit. **b** Key parameters of permanent magnet unit

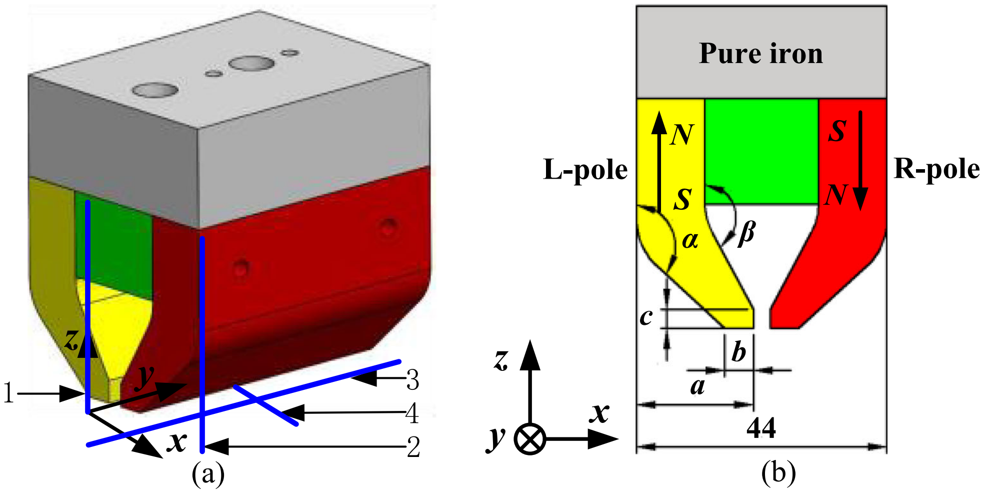

Table 1 Initial values of parameters for permanent magnet unit

a	*b*	*c*	*α*	*β*
20 mm	4 mm	3 mm	132.5°	147.5°

3 Material removal rate model

The material removal rate of Lap-MRF can be described by a linear relation of the pressure and velocity according to the Preston equation [18]:

$$R = kpv \tag{1}$$

where R is the material removal rate, k is the Preston coefficient related to polishing conditions other than the pressure and velocity such as material properties, abrasives, etc., p is the pressure between the polishing pad and the workpiece within the contact area, and v is the relative velocity between the polishing pad and the workpiece.

The kinematic relation of the polishing pad with eccentric rotation motion is shown in Fig. 4. O_1 is the center of the revolution motion, O_2 is the center of the spindle motion, g is the revolution radius, r_0 is the radius of the polishing pad, r is the distance between point A and O_1, n_1 is the revolution speed, and n_2 is the spindle speed.

The relative velocity distribution of the polishing pad on the workpiece at point A can be derived by the following equation [19]:

$$v(r) = \frac{n_2}{f}\int_{-\theta_0}^{\theta_0}\left[r^2(1+f)^2 + {r_0}^2 f^2 e^2 - 2rr_0 fe(1+f)\cos\theta\right]^{1/2}\mathrm{d}\theta \tag{2a}$$

where

$$\theta_0 = \arccos\left(\frac{r^2 + (e^2-1){r_0}^2}{2rer_0}\right),\ r\in[0, (1+e)r_0] \tag{2b}$$

where f is the speed ratio and $f = n_2/n_1$, and e is the eccentric ratio and $e = g/r_0$.

The pressure between the polishing pad and the workpiece within the contact area can be expressed as follows [20]:

$$p = \frac{3\varphi r_0 BH\beta^2 f_{\max}}{\pi h} = \frac{3\varphi r_0\beta^2 f_{\max}}{\pi}\cdot\frac{BH}{h} \tag{3a}$$

where

$$\beta = (\mu_i - \mu)/(\mu_i + 2\mu) \tag{3b}$$

Table 2 Plan of simulation experiments and summary of response parameters

Exp. no.	Simulation experimental conditions					Responses		Exp. no.	Simulation experimental conditions					Responses	
	a/mm	*b*/mm	*c*/mm	*α*/°	*β*/°	*Bh*/T	*Bl*/T		*a*/mm	*b*/mm	*c*/mm	*α*/°	*β*/°	*Bh*/T	*Bl*/T
1	20	2	3	132.5	155	0.42	0.092	22	20	4	1	132.5	155	0.44	0.093
2	19	4	3	125	147.5	0.49	0.097	23	20	2	3	140	147.5	0.33	0.084
3	20	2	5	132.5	147.5	0.43	0.089	24	20	6	3	132.5	155	0.53	0.095
4	20	6	3	125	147.5	0.57	0.095	25	19	4	3	132.5	155	0.47	0.091
5	20	6	3	132.5	140	0.51	0.093	26	21	4	3	125	147.5	0.54	0.097
6	20	4	5	140	147.5	0.45	0.092	27	19	6	3	132.5	147.5	0.47	0.093
7	20	2	3	132.5	140	0.36	0.090	28	20	6	5	132.5	147.5	0.59	0.094
8	19	4	5	132.5	147.5	0.47	0.093	29	21	4	3	132.5	140	0.46	0.093
9	19	2	3	132.5	147.5	0.42	0.092	30	21	2	3	132.5	147.5	0.40	0.09
10	20	4	1	132.5	140	0.45	0.093	31	20	4	1	125	147.5	0.44	0.095
11	21	6	3	132.5	147.5	0.54	0.092	32	20	4	3	125	140	0.49	0.093
12	20	4	3	125	155	0.52	0.097	33	21	4	3	140	147.5	0.42	0.088
13	21	4	5	132.5	147.5	0.50	0.092	34	19	4	1	132.5	147.5	0.39	0.093
14	20	2	3	125	147.5	0.42	0.092	35	20	4	1	140	147.5	0.37	0.087
15	20	4	5	132.5	140	0.48	0.092	36	20	2	1	132.5	147.5	0.34	0.09
16	20	4	3	132.5	147.5	0.47	0.090	37	20	4	3	140	155	0.47	0.087
17	20	6	1	132.5	147.5	0.46	0.093	38	20	4	5	125	147.5	0.54	0.098
18	19	4	3	140	147.5	0.43	0.089	39	20	4	3	140	140	0.41	0.087
19	21	4	3	132.5	155	0.49	0.093	40	19	4	3	132.5	140	0.39	0.088
20	20	4	5	132.5	155	0.51	0.093	41	20	6	3	140	147.5	0.50	0.087
21	21	4	1	132.5	147.5	0.43	0.089								

Table 3 Results of optimization

Solutions	*a*/mm	*b*/mm	*c*/mm	*α*/mm	*β*/°	*Bh*/°	*Bl*/°	Desirability
1	20.97	2.99	5.00	140.00	140.00	0.4245	0.0868	0.398
2	20.92	3.01	5.00	139.97	140.00	0.4246	0.0868	0.395
3	21.00	3.19	4.98	140.00	141.05	0.4339	0.0870	0.395
Selected	21.00	3	5.00	140.00	140	0.3877	0.0854	

where φ is the volume fractions of the magnetic particles in the MR fluid, B is the magnetic induction intensity of the MR fluid, H is the magnetic field intensity, μ is the magnetic permittivity of the MR fluid, μ_i is the magnetic permittivity of the magnetic particle, h is the working gap distance between the polishing lap and the workpiece, and f reaches a maximum $f_{\max} = 0.0571$ in the point dipole approximation.

Combining Eqs. (1), (2a) and (3a) produces the relationship for the material removal rate to the magnetic induction intensity of MR fluid, the magnetic field intensity, the working gap distance, and the spindle speed which can be expressed as follows:

$$R(r) = K(r)\frac{BH}{h}n_2 \tag{4}$$

where $K(r)$ is the coefficient related to polishing conditions.

Equation (4) shows that the material removal rate will increase with the enhancement of the magnetic field intensity in the H-field zones. Therefore, it is necessary to ensure the magnetic field intensity is as strong as possible in the H-field zones.

4 Permanent magnet unit optimization

From the above analysis in Section 2 and Section 3, we can see that we should enhance the magnetic field intensity in the H-field zones while weakening the magnetic field intensity in the L-field zones so as to improve the performance of Lap-MRF. Therefore, it is necessary to optimize the magnetic induction intensity distribution surrounding the permanent magnet unit.

Figure 5a shows that path 1 is beside the permanent magnet unit and along the center axis of the shaft, path 2 is on the symmetrical plane of the two adjacent permanent magnet units, path 3 is on the surface of the polishing lap and along the slice of the permanent magnet unit, and path 4 is on the surface of the polishing lap and perpendicular to the slice of the permanent magnet unit. These four paths are the special locations surrounding the permanent magnet unit. The magnetic induction intensity along path 1 and path 2 has important influence on the renewal of MR fluid, while the magnetic induction intensity along path 3 and path 4 has important influence on the material removal rate. Obviously, the five independent key parameters (i.e., a, b, c, α, and β as shown in Fig. 5b) would affect the magnetic induction intensity distribution along these four special paths. Figure 5b shows the x-z section plane of the permanent magnet unit. In order to optimize the five independent key parameters, the magnetic induction intensity distribution along the above four special paths under different five independent key parameters should be simulated and analyzed.

According to the properties of magnetic material, the magnetostatic simulation of the permanent magnet unit can be done using COMSOL Multiphysics 5.0 software. The initial values of the five independent key parameters for the permanent magnet unit are listed in Table 1.The material of the magnetic pole is Rubidium Iron Boron N52, whose remnant flux density is 14.3~14.8 kGs and coercive force is over 10.0 kOe. As Fig. 5b shows, the magnetizing direction of L-pole is along +z axis and the magnetizing direction of R-pole is along −z axis.

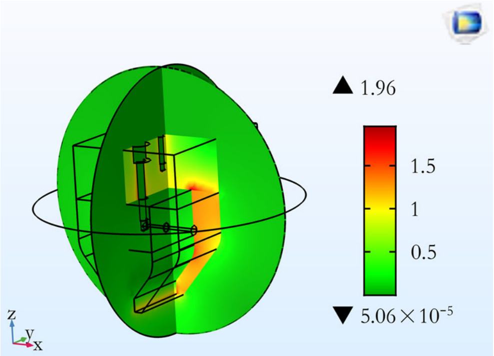

Fig. 6 Magnetic induction intensity distribution

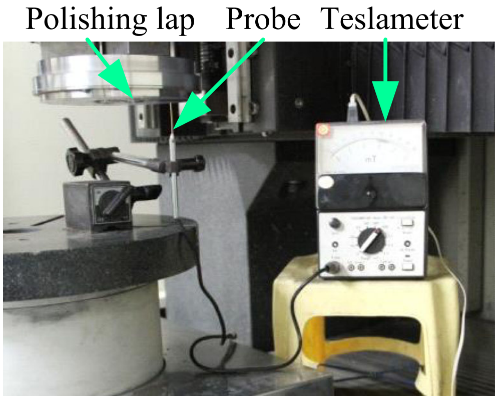

Fig. 7 Measurement system

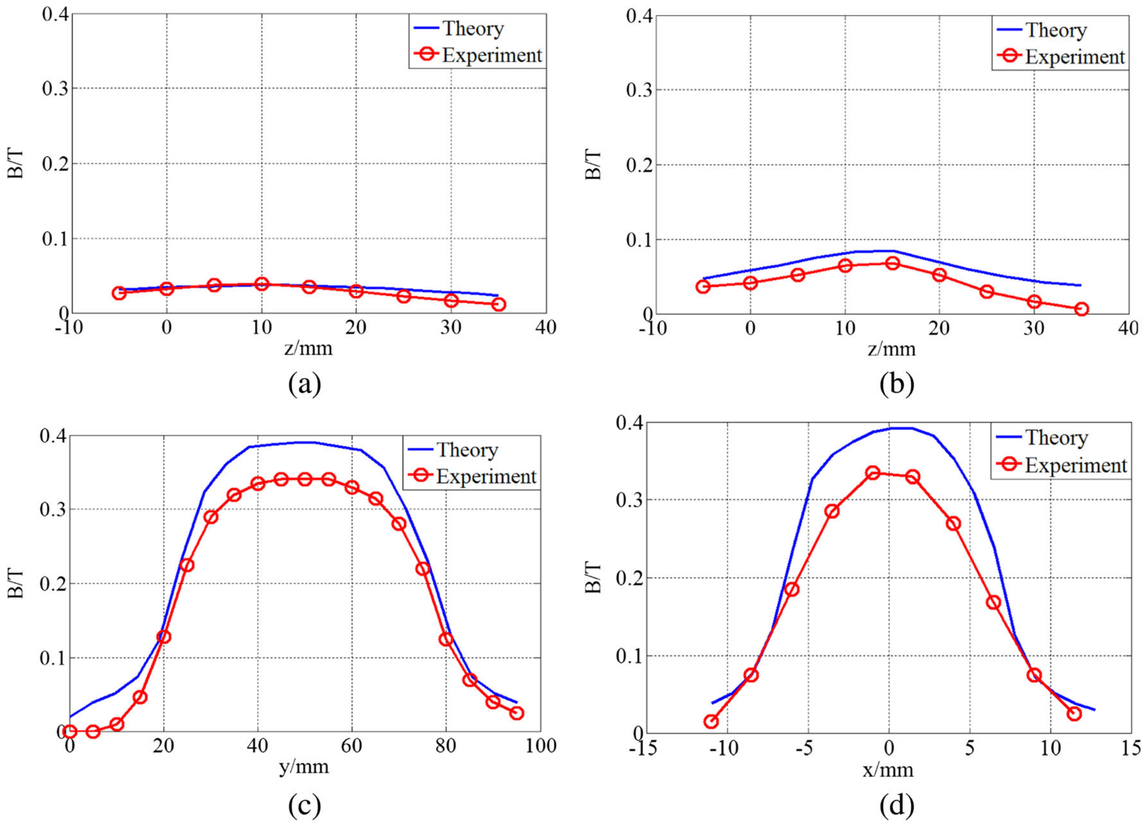

Fig. 8 Magnetic induction intensity curve along different paths. **a** Path 1. **b** Path 2. **c** Path 3. **d** Path 4

A detailed parameter study using Design Expert 8.0.6 software was conducted to evaluate the effect of the five independent key parameters on the magnetic induction intensity distribution surrounding the permanent magnet unit. In this study, the maximum magnetic induction intensity (*Bh*) along path 3 and path 4 and the maximum magnetic induction intensity (*Bl)* along path 1 and path 2 were selected as the two response parameters. Forty-one randomized simulation experimental conditions were designed according to the Box-Behnken design methodology with five factors which were varied over three levels. The values of the two response parameters (*Bh* and *Bl*) under 41 simulation experimental conditions were obtained using COMSOL Multiphysics. The randomized simulation experimental conditions and the summary of the two response parameters are given in Table 2. Based on the 41 randomized simulation experimental results, the functional relationship between the two response parameters and the five independent key parameters can be fitted as Eqs. (5) and (6), respectively.

$$Bh = 0.269 + 0.017a + 0.033b + 0.020c - 5.242 \times 10^{-3}a + 2.375 \times 10^{-3}\beta \tag{5}$$

$$Bl = 0.147 - 1.5 \times 10^{-4}a + 7.313 \times 10^{-4}b + 3.125 \times 10^{-4}c - 5.283 \times 10^{-4}a + 9.667 \times 10^{-5}\beta \tag{6}$$

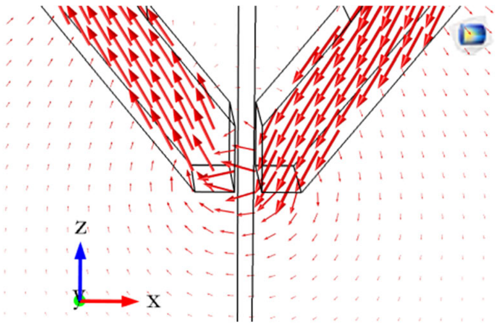

Fig. 9 Line of magnetic induction

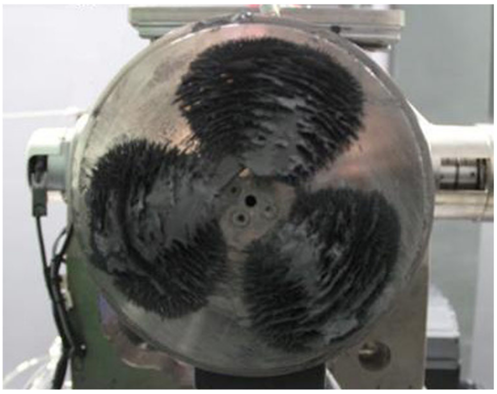

Fig. 10 MR fluid ribbons on polishing lap

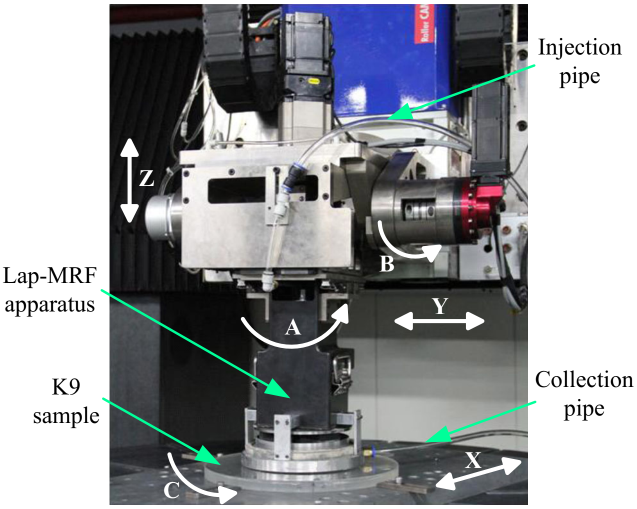

Fig. 11 Lap-MRF experimental set-up for polishing K9 sample

Table 5 Composition of MR fluid

Constituent	Volume concentration (%)
Carbonyl iron powder	40
Deionized water	56
Cerium oxide powder	2
Stabilizing agent	2

In order to improve the performance of Lap-MRF, a multi-objective optimization method was applied to optimize the five independent key parameters for the permanent magnet unit. The goal of the multi-objective optimization is that *Bh* should be as strong as possible while *Bl* should be as weak as possible. The objective functions for the multi-objective optimization are *Bh* and *Bl*, which are expressed as Eqs. (5) and (6), respectively. In order to meet the optimal design requirements and the structure size limitations, the values of each independent key parameter range from its minimum value to its maximum value, which are shown in Table 2. The mathematical model for the multi-objective optimization is as follows [21–23]:

$$\begin{cases} F(a,b,c,\alpha,\beta)=\min(-Bh,Bl) \\ Bh=0.269+0.017a+0.033b+0.020c-5.242\times10^{-3}\alpha+2.375\times10^{-3}\beta \\ Bl=0.147-1.5\times10^{-4}a+7.313\times10^{-4}b+3.125\times10^{-4}c-5.283\times10^{-4}\alpha+9.667\times10^{-5}\beta \\ 19\mathrm{mm}\le a\le 21\mathrm{mm} \\ 2\mathrm{mm}\le b\le 6\mathrm{mm} \\ 1\mathrm{mm}\le c\le 5\mathrm{mm} \\ 125^\circ\le\alpha\le140^\circ \\ 140^\circ\le\beta\le155^\circ \end{cases} \tag{7}$$

There are numerous methods used to solve multi-objective optimization problems [21, 24]. In this study, a method proposed by Derringer et al. was employed to identify the optimal combination of the five independent key parameters [25]. The optimization is performed in terms of the desirability function. The desirability functions of *Bh* and *Bl* are defined as follows, respectively.

$$d_\mathrm{h}=\begin{cases} 1, & Bh>Bh_\mathrm{max} \\ \left(\dfrac{Bh-Bh_\mathrm{min}}{Bh_\mathrm{max}-Bh_\mathrm{min}}\right)^r, & Bh_\mathrm{max}>Bh>Bh_\mathrm{min} \\ 0, & Bh<Bh_\mathrm{min} \end{cases} \tag{8}$$

$$d_\mathrm{l}=\begin{cases} 0, & Bl>Bl_\mathrm{max} \\ \left(\dfrac{Bl_\mathrm{max}-Bl}{Bl_\mathrm{max}-Bl_\mathrm{min}}\right)^r, & Bl_\mathrm{max}>Bl>Bl_\mathrm{min} \\ 1, & Bl<Bl_\mathrm{min} \end{cases} \tag{9}$$

where Bh_max, Bh_min and Bl_max, Bl_min are the maximum and minimum values of *Bh* and *Bl*, respectively, from the simulation experimental results. Considering the linear increment of desirability, $r = 1$ is selected. The geometric mean of d_h and d_l is then used to assess the desirability *D* of the combined response levels [25]. Then, *F* in Eq. (7) can be defined as Eq. (10) and the maximum value of desirability *D* corresponds to the minimum value of *F*.

$$F(a,b,c,\alpha,\beta)=\min\{-D\}=\min\left\{-(d_\mathrm{h},d_\mathrm{l})^{1/2}\right\} \tag{10}$$

Table 4 Experimental parameters of Lap-MRF

n_1 (rpm)	n_2 (rpm)	$e=g/r_0$	Q (L/h)	h (mm)	t (h)
0	100	0	80	1.8	0.5

Combining Eqs. (7), (8), (9), and (10), the desirability *D* for each level of the five independent key parameters can be obtained. The Design Expert 8.0.6 software was used to search the maximum desirability *D*. The first three optimization solutions for maximizing *Bh* and minimizing *Bl* are listed in Table 3. We select the average value of the each independent parameter as the optimal key parameter, and the final values of the five independent key parameters are listed in Table 3.

The simulation result of the magnetic induction intensity distribution in the two symmetrical planes after optimization

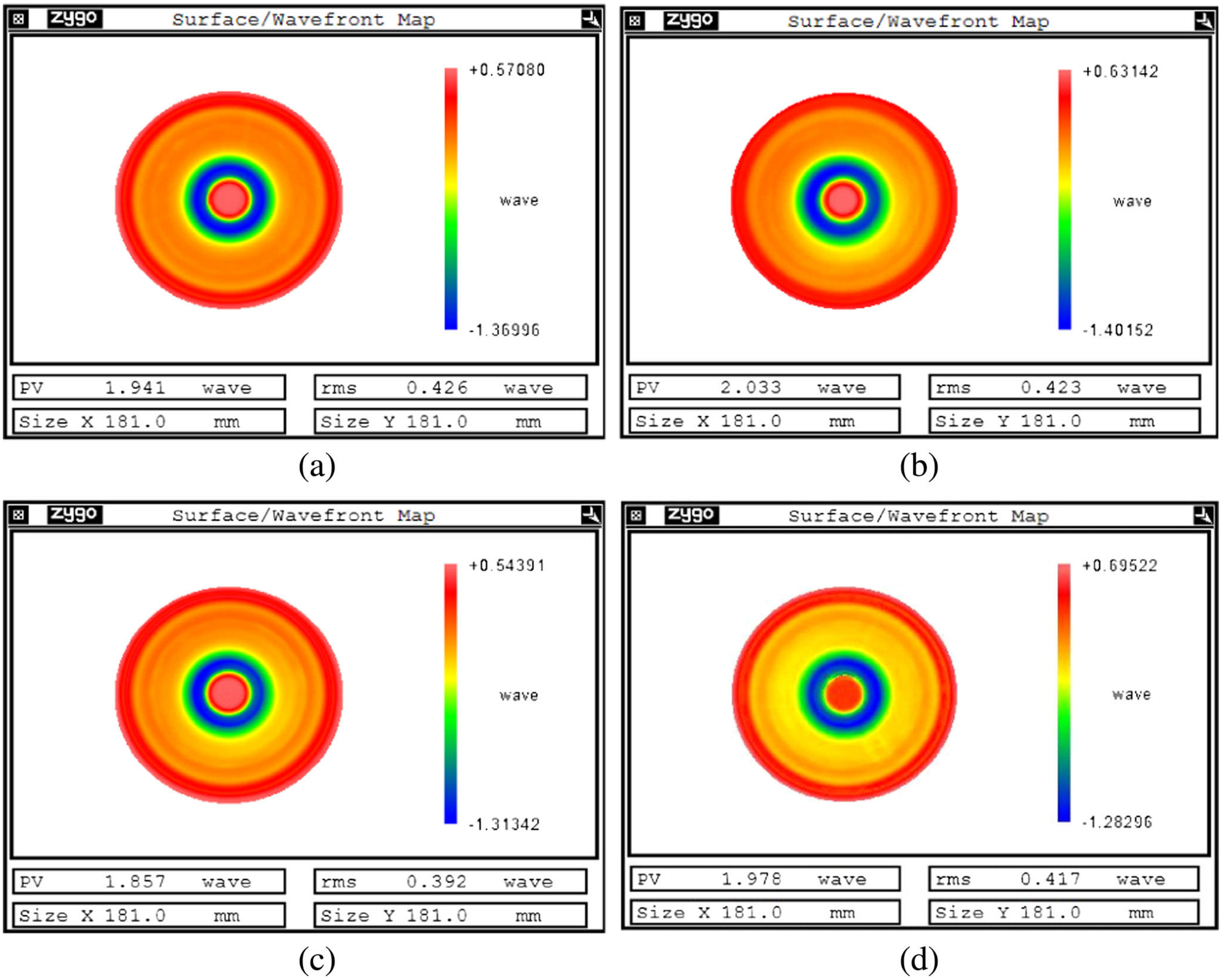

PV 1.941 wave
rms 0.426 wave
Size X 181.0 mm
Size Y 181.0 mm

(a)

PV 2.033 wave
rms 0.423 wave
Size X 181.0 mm
Size Y 181.0 mm

(b)

PV 1.857 wave
rms 0.392 wave
Size X 181.0 mm
Size Y 181.0 mm

(c)

PV 1.978 wave
rms 0.417 wave
Size X 181.0 mm
Size Y 181.0 mm

(d)

Fig. 12 The removal function shape ($\lambda = 632.8$ nm). **a** The first removal function. **b** The second removal function. **c** The third removal function. **d** The fourth removal function

is shown in Fig. 6. Figure 7 shows the measurement system we used to measure the magnetic induction intensity distribution along different paths. The polishing device was mounted on a numerically controlled machine tool developed by our research group, so we could easily measure magnetic induction intensity distribution along different paths. The model of the teslameter used in the measurement is PG-5A.

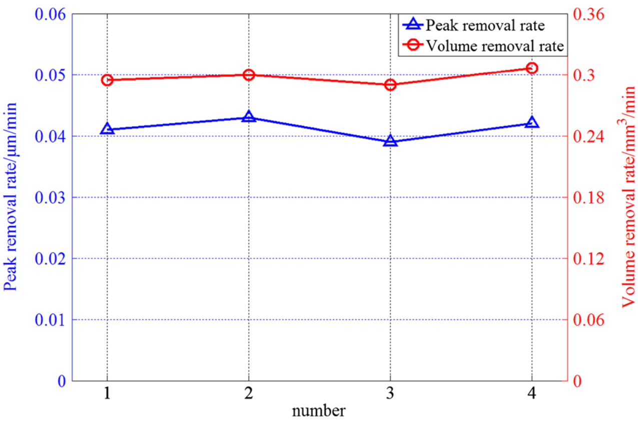

Fig. 13 The variation curve of the material removal rate

Figure 8a–d shows the simulation results and the measurement results of the magnetic induction intensity distribution along the above four paths, respectively. From these figures, we can see that the measurement results are in good agreement with the theoretical simulation results, which verifies the accuracy of the simulation.

The distribution of the line of magnetic induction is shown in Fig. 9. The line of magnetic induction bulges over the poles

Table 6 Experimental parameters of MRF (wheel diameter 200 mm)

Wheel speed	Flow of MR fluid	Insertion depth
240 rpm	140 L/h	0.25 mm

Table 7 Experimental parameters of Lap-MRF

n_1 (rpm)	n_2 (rpm)	$e = g/r_0$	Q (L/h)	h (mm)
120	125	0.5	80	1

and the magnetic field gradient is normal to the polishing lap which is beneficial to the formation of the MR fluid ribbon [26]. As shown in Fig. 10, there exist three stable MR fluid ribbons below the permanent magnet units along the radial direction of the polishing lap; however, there is not much MR fluid which is pressed against the polishing lap between any two adjacent permanent magnet units.

From above analysis, it can be seen that the magnetic induction intensity in the H-field zones is up to 0.35 T so that the MR fluid can come into a viscoplastic Bingham medium and form ribbon protrusions to polish the workpiece, while the magnetic induction intensity in the L-field zones is under 0.08 T so that MR fluid can flow freely to achieve renewal, which can satisfy the using requirements.

5 Experiments

5.1 Material removal rate stability

Higher material removal rate stability in a long-time polishing process is necessary for processing large aperture mirrors. The material removal rate of Lap-MRF is affected by such parameters as the MR fluid, the abrasive particle size, the abrasive particle type, the magnetic field intensity, the relative velocity between the polishing pad and the workpiece, the working gap distance between the polishing lap and the workpiece, and so on. In this paper, we performed experiments on K9 sample for four times under the same experimental parameters to validate the stability and repeatability of the removal functions. In accordance with an actual fabrication situation, the Lap-MRF experimental set-up was still under use for polishing another K9 sample during the interval (5 h) between any two adjacent removal functions. The photograph of Lap-MRF experimental set-up for polishing K9 sample is shown in Fig. 11. The whole experimental set-up is modified on a numerically controlled machine tool developed by our research group. The relative motion between the experimental set-up and the workpiece can be controlled on six axes: X, Y, Z, A, B, and C. The experimental parameters are given in Table 4. Q is the flow rate of the MR fluid. t is the polishing time for each removal function. The diameter of the polishing lap is 165 mm. The MR fluid used in the experiments is water-based MR fluid and its composition is listed in Table 5.

The size of K9 sample used in the former experiments is Φ350 mm × 20 mm. The K9 samples were all initially prepared using CCOS with cerium oxide abrasives. We measured the surface profile by 24-in. Zygo interferometer before and after polishing and then obtained the removal functions as shown in Fig. 12. Figure 13 shows the variation curve of the peak and volume removal rate of different removal functions, and the stability of the volume removal rate is less than 5.5%. As a contrast, the variation ratio of volume removal rate is about 10~20% for CCOS [27–29]. Lap-MRF is of better material removal stability than CCOS, which can be used for surface figuring.

5.2 Surface roughness improvement

Lap-MRF uses flexible MR fluid as polishing pad and the polishing pad can execute planetary motion so that the smooth surface can be obtained. In order to verify the improvement of surface roughness, we performed experiments on K9 samples and silicon modification layers on silicon carbide substrates using MRF and Lap-MRF. The silicon modification layers on the silicon carbide substrates were prepared using the modification technology of ion beam-assisted deposition. The initial surface roughness of two K9 samples and two silicon modification layers on two silicon carbide substrates were almost the

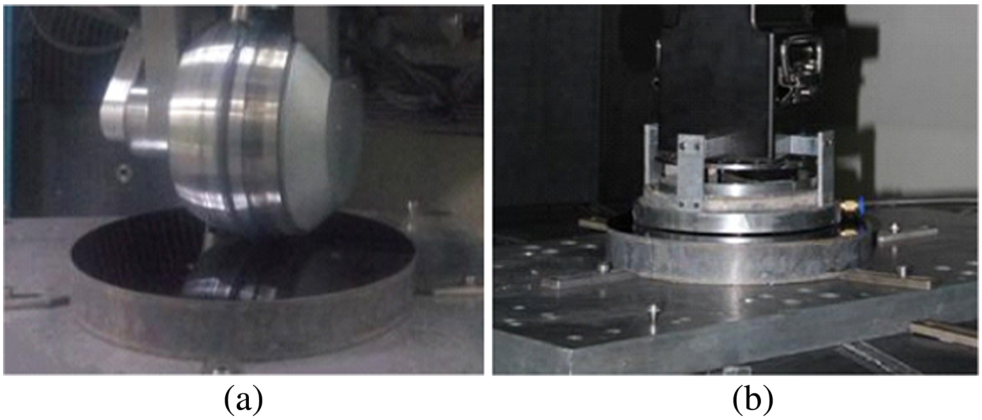
(a) (b)

Fig. 14 Experimental set-ups for polishing a silicon modification layer. **a** MRF. **b** Lap-MRF same, respectively. They were all initially prepared using CCOS with cerium oxide abrasives. The MR fluid used in MRF was the same with that used in Lap-MRF. The experimental parameters of MRF and Lap-MRF are given in Table 6 and Table 7, respectively. For two K9 samples, the final surface roughness after polishing using MRF is almost the same as that after polishing using Lap-MRF. However, great difference takes place when polishing silicon modification layers using MRF and Lap-MRF, respectively. The photograph of MRF and Lap-MRF experimental set-ups for polishing silicon modification layers are shown in Fig. 14a, b, respectively.

The RMS surface roughness was measured using the Zygo white-light interferometer with × 10 lens. The initial and final surface roughness for silicon modification layer before and after polishing using MRF is shown in Fig. 15a, b, respectively. The initial and final surface roughness for silicon modification layer before and after polishing using Lap-MRF is shown in Fig. 15c, d, respectively. For the silicon modification layer after polishing using MRF, there exist deep pits that are polished into a comet-like form by the MR fluid which deteriorates the finished surface roughness. The RMS value of surface roughness deteriorates to 2.051 nm from 1.690 nm after polishing using MRF. For the silicon modification layer after polishing using Lap-MRF, however, the deep pit vanishes and the polishing ripple is not apparent. The RMS value of surface roughness is improved to 0.788 nm from 1.610 nm after polishing using Lap-MRF, which verifies the improvement of surface roughness of silicon modification layer using Lap-MRF.

5.3 Simulation process for a large aperture mirror

The material removal amount for large aperture mirrors increases greatly, so that higher material removal rate and convergence are required to shorten the processing cycle. In order to verify the convergence using Lap-MRF, we performed simulation process using the Lap-MRF removal function of K9 on a Φ1000-mm flat. The initial surface shape of Φ1000 mm with

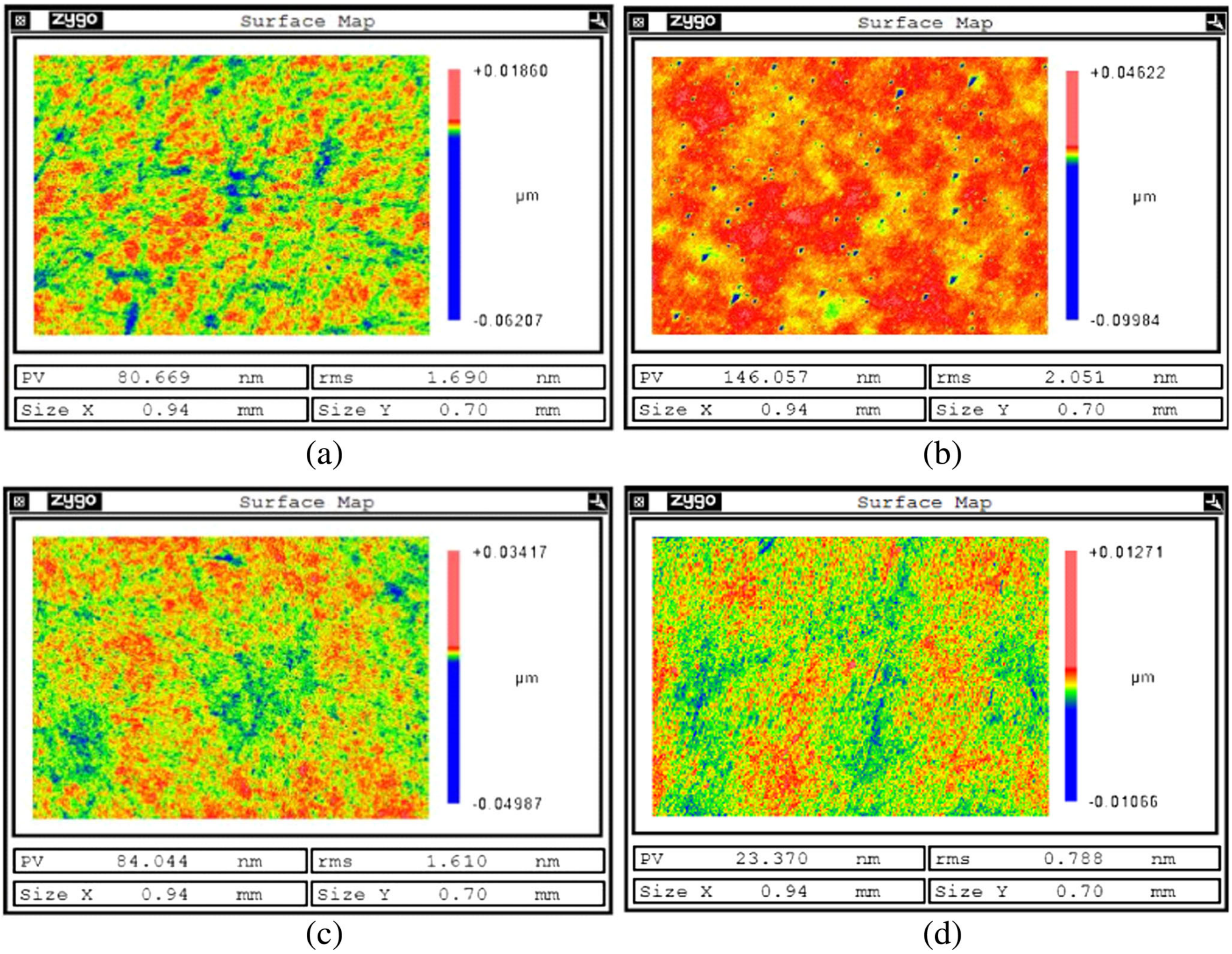

PV 80.669 nm | rms 1.690 nm
Size X 0.94 mm | Size Y 0.70 mm

(a)

PV 146.057 nm | rms 2.051 nm
Size X 0.94 mm | Size Y 0.70 mm

(b)

PV 84.044 nm | rms 1.610 nm
Size X 0.94 mm | Size Y 0.70 mm

(c)

PV 23.370 nm | rms 0.788 nm
Size X 0.94 mm | Size Y 0.70 mm

(d)

Fig. 15 The surface roughness for silicon modification layer before and after MRF and Lap-MRF. **a** Surface roughness before MRF. **b** Surface roughness after MRF. **c** Surface roughness before Lap-MRF. **d** Surface roughness after Lap-MRF

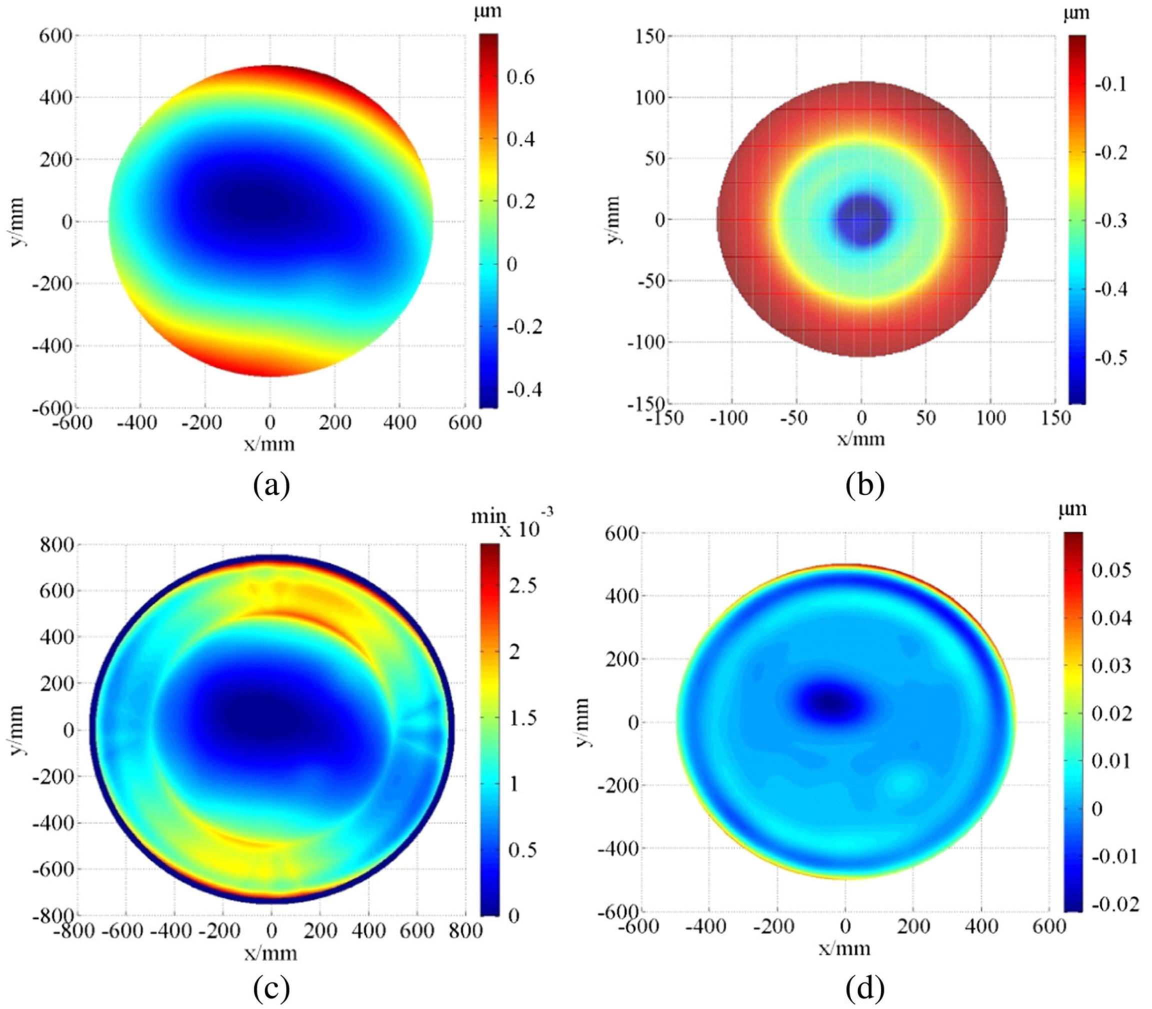

Fig. 16 Simulation process for a Φ1000-mm mirror. **a** Initial surface shape. **b** Remove function. **c** Dwell time distribution. **d** Final surface shape

1.2 μm PV (peak-to-valley) and 0.26 μm RMS is shown in Fig. 16a. Figure 16b shows the Lap-MRF removal function of K9 which is obtained under the same experimental parameters as given in Table 7 and the polishing time is 10 min. The volume removal rate for this removal function is up to 0.76 mm^3/min. When calculating the dwell time, we changed the mirror into a Φ1450-mm flat using image extension to avoid the ring effect. The dwell time on a Φ1450-mm flat is shown in Fig. 16c. During the simulation process, we adopted the raster tool path. Moreover, the edge effect and location error are both ignored. The final surface shape after simulation process is shown in Fig. 16d. The surface shape is converged to 0.0795 μm PV and 0.0073 μm RMS after 501 min polishing and the convergence efficiency is 97.2%. However, the volume removal rate of MRF for K9 is 0.24 mm^3/min under the same experimental parameters as given in Table 6. When we performed simulation process using MRF, the same initial surface shape is converged to 0.0645 μm PV and 0.0013 μm RMS after 1618 min polishing and the convergence efficiency is 99.5%. Although the convergence efficiency of Lap-MRF is a little bit smaller than that of MRF, the polishing time of Lap-MRF is shorter than one third of the MRF polishing time.

6 Conclusion

To combine the advantages of CCOS and MRF, a kind of novel Lap-MRF method has been proposed. For Lap-MRF, the MR fluid in the polishing zones can be renewed continuously to ensure the stability of the material removal efficiency and a lap is used to improve the material removal rate largely. Moreover, Lap-MRF uses flexible MR fluid as polishing pad so as to match the surface well and the polishing pad executes planetary motion to achieve high-quality process. The main conclusions in this paper are as follows:

1. The magnetic induction intensity should be as strong as possible in H-field zones and as weak as possible in L-field zones to improve the performance of Lap-MRF.

After simulation and optimization of the permanent magnet unit, the magnetic field intensity in H-field zones is up to 0.35 T so that the MR fluid can form ribbon protrusions to polish the workpiece, while the magnetic field intensity in the L-field zones is under 0.08 T so that the MR fluid can flow freely to achieve renewal.

2. The material removal rate of Lap-MRF is stable. Four removal functions on K9 sample are taken. The relative change rate of the volume removal rate is less than 5.5% using Lap-MRF comparing to 10~20% using CCOS, which makes Lap-MRF capable of surface figuring.
3. Smooth surface is obtained using Lap-MRF. For silicon modification layer, the surface roughness is improved to 0.788 nm RMS from 1.610 nm RMS using Lap-MRF, while it deteriorates to 2.051 nm RMS from 1.690 nm RMS using MRF. There is not any deep pit and apparent polishing ripple on the surface. As a result, smooth surface can be obtained.
4. Lap-MRF is of better processing efficiency and convergence. The volume removal rate for K9 is up to 0.76 mm^3/min using Lap-MRF comparing to 0.24 mm^3/min using MRF. When using MATLAB simulation process method, the polishing time for a Φ1000-mm mirror decreases to 501 min and the convergence efficiency is 97.2% using Lap-MRF comparing to 1618 min and 99.5% using MRF.

Acknowledgments The authors want to express their gratitude to professors and students from Hu'nan Key Laboratory of Ultra-precision Machining Technology for their helpful participation.

Funding information This project is supported by National Natural Science Foundation of China (NSFC) (51405503), National Natural Science Foundation of China (NSFC) (5167051486), National Natural Science Foundation of China (NSFC) (91523101) and the national key research and development plan of China (No. 2016YFB1102304).

References

1. Geyl R (2005) From VLT to GTC and the ELTs. Proc SPIE 5965: 59650P. https://doi.org/10.1117/12.627677
2. Martin HM, Burge JH, Cuerden B, Davison WB, Kingsley JS (2008) Progress in manufacturing the first 8.4 m off-axis segment for the Giant Magellan Telescope. Proc SPIE 7018:70180C. https://doi.org/10.1117/12.789805
3. Allen LN, Hannon JJ, Wambach RW (1992) Final surface error correction of an off-axis aspheric petal by ion figuring. Proc SPIE 1543:190–200. https://doi.org/10.1117/12.51181
4. Wan YJ, Shi CY, Yuan JH, Wu F (2011) Control method of polishing errors by dwell time compensation. High Power Laser and Particle Beams 23(1):97–100, in Chinese. https://doi.org/10.3788/HPLPB20112301.0097
5. Song C, Walker D, Yu G (2011) Misfit of rigid tools and interferometer subapertures on off-axis aspheric mirror segments. Opt Eng 50(7):073401. https://doi.org/10.1117/1.3597328
6. Kordonski WI, Golini D (1999) Fundamentals of magnetorheological fluid utilization in high precision finishing. J Intell Mater Syst Struct 10(9):683–689. https://doi.org/10.1106/011M-CJ25-64QC-F3A6
7. Jacobs SD, Kordonski WI, Prokhorov IV, Golini D, Gorodkin GR, Strafford TD(1998) Deterministic magnetorheological finishing. U.S. Patent No. 5795212
8. Golini D, Schneider G, Flug P, Demarco M (2001) The ultimate flexible optics manufacturing technology: magnetorheological finishing. Opt Photon News 12(10):20–24. https://doi.org/10.1364/OPN.12.10.000020
9. DeGroote JE (2007) Surface interactions between nanodiamonds and glass in magnetorheological finishing (MRF). Doctor Degree Dissertation, University of Rochester
10. Ren K, Luo X, Zheng LG, Bai Y, Li LX, HX H, Zhang XJ (2014) Belt-MRF for large aperture mirrors. Opt Express 22(16):19262–19276. https://doi.org/10.1364/OE.22.019262
11. Pan JS, Yan QS, Lu JB, Xu XP, Chen SK (2014) Cluster magnetorheological effect plane polishing technology. J Mech Eng 50(01):205–212, in Chinese. https://doi.org/10.3901/JME.2014.01.205
12. Pan JS, Yan QS (2015) Material removal mechanism of cluster magnetorheological effect in plane polishing. Int J Adv Manuf Technol 81(9-12):2017–2026. https://doi.org/10.1007/s00170-015-7332-7
13. Guo ZD, Du SJ, Liu WG, Hang LX, Wang W (2007) The application of annulus magnetic field in magnetorheological finishing. J Xi'an Technol Univ 27(3):212–214, in Chinese. https://doi.org/10.3969/j.issn.1673-9965.2007.03.003
14. Singh AK, Jha S, Pandey PM (2013) Mechanism of material removal in ball end magnetorheological finishing process. Wear 302(1-2):1180–1191. https://doi.org/10.1016/j.wear.2012.11.082
15. Jha S, Jain VK, Komanduri R (2007) Effect of extrusion pressure and number of finishing cycles on surface roughness in magnetorheological abrasive flow finishing (MRAFF) process. Int J Adv Manuf Technol 33(7):725–729. https://doi.org/10.1007/s00170-006-0502-x
16. Das M, Jain VK, Ghoshdastidar PS (2008) Fluid flow analysis of mgnetorheological abrasive flow finishing (MRAFF) process. Int J Adv Manuf Technol 38(5):613–621. https://doi.org/10.1016/j.ijmachtools.2007.09.004
17. Guo HR, YB W, Lu D, Fujimoto M, Nomura M (2014) Effects of pressure and shear stress on material removal rate in ultra-fine polishing of optical glass with magnetic compound fluid slurry. J Mater Process Technol 214(11):2759–2769. https://doi.org/10.1016/j.jmatprotec.2014.06.014
18. Preston F (1927) The theory and design of plate glass polishing machines. J Soc Glas Technol 9(2):14–256
19. Nam HS, Kim GC, Kim HS, Rhee HG, Ghim YS (2016) Modeling of edge tool influence functions for computer controlled. Int J Adv Manuf Technol 83(5-8):911–917. https://doi.org/10.1007/s00170-015-7633-x
20. Guo CY, Gong XL, Xuan SH, Qin LJ, Yan QF (2013) Compression behaviors of magnetorheological fluids under nonuniform magnetic field. Rheol Acta 52(2):165–176. https://doi.org/10.1007/s00397-013-0678-6
21. Karpat Y, Özel T (2007) Multi-objective optimization for turning processes using neural network modeling and dynamic-neighborhood particle swarm optimization. Int J Adv Manuf Technol 35(3-4):234–247. https://doi.org/10.1007/s00170-006-0719-8
22. Liu SH (2015) Multi-objective optimization design method for the machine tool's structural parts based on computer-aided engineering. Int J Adv Manuf Technol 78(5-8):1053–1065. https://doi.org/10.1007/s00170-014-6700-z
23. Wei Z, Feng YX, Tan JR, Wang JL, Li ZK (2009) Multi-objective performance optimal design of large-scale injection molding

machine. Int J Adv Manuf Technol 41(3-4):242–249. https://doi.org/10.1007/s00170-008-1467-8

24. Marler RT, Arora JS (2004) Survey of multi-objective optimization methods for engineering. Struct Multidiscip Optim 26(6):369–395. https://doi.org/10.1007/s00158-003-0368-6
25. Derringer G, Suich R (1980) Simultaneous optimization of several response variables. J Qual Technol 12:214–219
26. Zhang FD, Zhang XJ, Y JC (2000) Mathematics model of magnetorheological finishing. Proc SPIE 4231:490–497. https://doi.org/10.1117/12.402796
27. Kim DW, Burge JH (2010) Rigid conformal polishing tool using non-linear visco-elastic effect. Opt Express 18(3):2242–2257. https://doi.org/10.1364/OE.18.002242
28. Dong ZC, Cheng HB (2014) Study on removal mechanism and removal characters for SiC and fused silica by fixed abrasive diamond pellets. Int J Mach Tool Manu 85:1–13. https://doi.org/10.1016/j.ijmachtools.2014.04.008
29. Nie XQ (2014) Study on the smoothing polishing mechanism and process of mid-spatial frequency error for high accuracy optics. Doctor Degree Dissertation, National University of Defense Technology, in Chinese